Monthly Notices of the ROYAL ASTRONOMICAL SOCIETY
MNRAS **545,** 1–8 (2026) https://doi.org/10.1093/mnras/staf2022

Discovery of a $z \sim 0.8$ ultra steep spectrum radio halo in the MeerKAT-South Pole Telescope Survey

Isaac S. Magolego,[1★] Roger P. Deane,[1,2] Kshitij Thorat,[2] Ian Heywood,[3,4,5] William Rasakanya,[1] Manuel Aravena,[6,7] Lindsey E. Bleem,[8,9,10] Maria G. Campitiello,[8] Kedar A. Phadke,[11,12,13] Justin Spilker,[14] Joaquin D. Vieira,[11,12] Dazhi Zhou,[15] Bradford A. Benson,[9,10,16] Scott Chapman,[17,18,19] Ana Posses,[14] Tim Schrabback,[20] Antony Stark[21] and David Vizgan[11]

[1]*Wits Centre for Astrophysics, School of Physics, University of the Witwatersrand, Private Bag 3, 2050 Johannesburg, South Africa*
[2]*Department of Physics, University of Pretoria, Hatfield, Pretoria 0028, South Africa*
[3]*Astrophysics, Department of Physics, University of Oxford, Keble Road, Oxford OX1 3RH, UK*
[4]*Department of Physics and Electronics, Rhodes University, PO Box 94, Makhanda 6140, South Africa*
[5]*South African Radio Astronomy Observatory, 2 Fir Street, Observatory 7925, South Africa*
[6]*Instituto de Estudios Astrofícos, Facultad de Ingeniería y Ciencias, Universidad Diego Portales, Av. Ejército 441, Santiago 8370191, Chile*
[7]*Millenium Nucleus for Galaxies (MINGAL), Concepción 4030000, Chile*
[8]*High-Energy Physics Division, Argonne National Laboratory, 9700 South Cass Avenue., Lemont, IL 60439, USA*
[9]*Kavli Institute for Cosmological Physics, University of Chicago, 5640 South Ellis Avenue, Chicago, IL 60637, USA*
[10]*Department of Astronomy and Astrophysics, University of Chicago, 5640 South Ellis Avenue, Chicago, IL 60637, USA*
[11]*Department of Astronomy, University of Illinois, 1002 West Green Street, Urbana, IL 61801, USA*
[12]*Center for AstroPhysical Surveys, National Center for Supercomputing Applications, Urbana, IL 61801, USA*
[13]*NSF-Simons AI Institute for the Sky (SkAI), 172 E. Chestnut St., Chicago, IL 60611, USA*
[14]*Department of Physics and Astronomy and George P. and Cynthia Woods Mitchell Institute for Fundamental Physics and Astronomy, Texas A&M University, 4242 TAMU, College Station, TX 77843-4242, USA*
[15]*Department of Physics and Astronomy, University of British Columbia, 6225 Agricultural Road, Vancouver V6T 1Z1, Canada*
[16]*Fermi National Accelerator Laboratory, MS209, P.O. Box 500, Batavia, IL 60510-0500, USA*
[17]*Department of Physics and Astronomy, University of British Columbia, 6225 Agricultural Road, Vancouver V6T 1Z1, Canada*
[18]*National Research Council, Herzberg Astronomy and Astrophysics, 5071 West Saanich Road, Victoria V9E 2E7, Canada*
[19]*Department of Physics and Atmospheric Science, Dalhousie University, 6310 Coburg Road, Halifax B3H 4R2, Canada*
[20]*Institut für Astro- und Teilchenphysik, Universität Innsbruck, Technikerstr. 25/8, A-6020 Innsbruck, Austria*
[21]*Harvard-Smithsonian Center for Astrophysics, 60 Garden Street, Cambridge, MA 02138, USA*

Accepted 2025 November 11. Received 2025 November 11; in original form 2025 September 9

ABSTRACT

Radio haloes are diffuse synchrotron sources that trace the turbulent intracluster medium (ICM) of galaxy clusters. However, their origin remains unknown. Two main formation models have been proposed: the hadronic model, in which relativistic electrons are continuously injected by cosmic-ray protons; and the leptonic turbulent re-acceleration model, where cluster mergers re-energize electrons *in situ*. A key discriminant between the two models would be the existence of ultra-steep spectrum radio haloes (USSRHs), which can only be produced through turbulent re-acceleration. Here, we report the discovery of an USSRH in the galaxy cluster SPT-CLJ2337−5942 at redshift $z = 0.78$ in the MeerKAT-South Pole Telescope 100 deg^2 UHF (0.58–1.09 GHz) survey. This discovery is noteworthy for two primary reasons: it is the highest redshift USSRH system to date; and the close correspondence of the radio emission with the thermal ICM as traced by *Chandra* X-ray observations, further supporting the leptonic re-acceleration model. The halo is underluminous for its mass, consistent with a minor merger origin, which produces steep-spectrum, lower luminosity haloes. This result demonstrates the power of wide-field, high-fidelity, low-frequency ($\lesssim$ 1 GHz) surveys like the MeerKAT-SPT 100 deg^2 programme to probe the origin and evolution of radio haloes over cosmic time, ahead of the Square Kilometre Array.

Key words: galaxies: clusters: general – radio continuum: general – X-rays: galaxies – X-rays: galaxies: clusters.

1 INTRODUCTION

Galaxy clusters are the largest gravitationally bound structures in the universe. Their halo masses are of order $10^{14–15}$ M$_\odot$ and are primary nodes in the cosmic web, a network of galaxy-filled filaments stretching across tens to hundreds of megaparsecs (Mpc; M. A. Aragón-Calvo, R. Van De Weygaert & B. J. T. Jones 2010; M. Cautun et al. 2014; N. Malavasi et al. 2020). Clusters are important cosmic laboratories for both astrophysics and cosmology. They are predominately comprised of dark matter, which accounts for about 70–80 per cent of their mass, while 15–20 per cent is hot

★ E-mail: isaacike07@gmail.com

(10^{6-7} K) ionized gas known as the intracluster medium (ICM; G. R. Blumenthal et al. 1984; D. A. White & A. C. Fabian 1995; C. Jones & W. Forman 1999; A. Vikhlinin et al. 2006; M. A. Aragón-Calvo et al. 2010). The remaining fraction lies within stars and galaxies. Occasionally, clusters collide and merge in powerful events, releasing huge amounts of energy ($\sim 10^{64}$ erg) over time-scales of order several Gyr. This energy creates shocks and turbulence that heat the ICM, which can leave signatures of the cluster merger activity (M. Markevitch & A. Vikhlinin 2007). Based on their state, clusters can be classified as either 'relaxed' (undisturbed), or 'merging' (disturbed), which are disturbed by these energetic interactions (M. Markevitch & A. Vikhlinin 2007; A. W. Mann & H. Ebeling 2012; Z. S. Yuan & J. L. Han 2020). One complementary approach to studying a cluster's dynamics is by detecting diffuse radio synchrotron emission, generated in the presence of large-scale weak magnetic fields ($\sim 1\,\mu$G), that extend across cluster environments. This emission, typically classified as radio haloes and relics, is often associated with merger activity within the cluster (e.g. L. Feretti et al. 2012; G. Brunetti & T. W. Jones 2014; R. J. Weeren et al. 2019).

Radio relics are elongated structures typically found at the outskirts of galaxy clusters. They exhibit polarized emission and their elongation (major axis) is oriented perpendicular to the line connecting the relic to the cluster centre. These relics, typically found in disturbed systems (R. J. Weeren et al. 2019, and references therein), challenge our understanding as they have physical sizes (Mpc-scale) significantly larger than expected considering the radiative lifespan ($t \sim 10$–100 Myr) of radiating particles emitting at radio wavelengths (J. Bagchi et al. 2002). These characteristics suggest a cluster merger origin, where particles are re-energized through resultant shocks, one proposed mechanism for which is diffusive shock acceleration (DSA; T. Ensslin et al. 1998; K. Roettiger, J. O. Burns & J. M. Stone 1999). However, several observational and theoretical challenges remain in reconciling radio relic properties with the standard DSA scenario of thermal electron acceleration (e.g. G. Brunetti & T. W. Jones 2014; R. J. Weeren et al. 2019). In particular, (a) the low Mach numbers inferred from X-ray observations are often inconsistent with the acceleration efficiencies predicted by such DSA models (G. Macario et al. 2011; A. Botteon et al. 2020; D. Wittor et al. 2021; J. Whittingham et al. 2024); (b) some clusters exhibiting clear X-ray shocks show no associated relic emission (e.g. H. R. Russell et al. 2011; S. Dasadia et al. 2016); and (c) the observed alignment and ordering of magnetic fields in certain relics deviate from theoretical expectations (R. J. Weeren et al. 2010). These issues highlight that while DSA likely operates at cluster shocks, additional processes such as re-acceleration of fossil electrons or complex magnetic field geometries may also play significant roles.

In contrast, radio haloes are diffuse synchrotron emission components that span approximately a megaparsec in size, primarily co-located at the centre of the galaxy clusters. Their surface brightness typically measures in the range of a few μJy/arcsec^2 at 0.1–1 GHz, making them orders of magnitude fainter compared to their relic counterparts. These haloes have been identified in $\sim$50 high-mass clusters (e.g. R. J. Weeren et al. 2019, and references therein), mostly at low to intermediate redshift ($z \lesssim 0.4$), with only a few identified beyond $z \approx 0.5$ (see Z. S. Yuan, J. L. Han & Z. L. Wen 2015; V. Cuciti et al. 2021a; T. Pasini et al. 2024; D. G. Phuravhathu et al. 2025, for details and additional references). Similar to radio relics, the observed scales of radio haloes suggest a need for particle re-acceleration (R. Cassano, M. Gitti & G. Brunetti 2008b). Two leading theoretical models are the hadronic or secondary-electron model, where relativistic electrons are generated from proton–proton collisions within the ICM (B. Dennison 1980; P. Blasi & S. Colafrancesco 1999); and the turbulent re-acceleration model. The latter asserts that an existing population of cosmic ray electrons undergoes re-acceleration due to turbulence generated by cluster mergers (G. Brunetti et al. 2001; V. Petrosian 2001; R. Cassano & G. Brunetti 2005; G. Brunetti & A. Lazarian 2007; F. Miniati 2015; K. Nishiwaki & K. Asano 2022). While the possibility of combining the two models has not been excluded (G. Brunetti & P. Blasi 2005; G. Brunetti & A. Lazarian 2011; R. Cassano et al. 2012), the turbulent re-acceleration model is currently favoured (L. Bruno et al. 2021; S. W. Duchesne, M. Johnston-Hollitt & A. G. Wilber 2021; R. Cassano et al. 2023; K. Rajpurohit et al. 2023; E. Osinga et al. 2025). This preference arises from several key observational tensions with the hadronic model. First, the expected level of gamma-ray emission associated with neutral pion decay (a byproduct of hadronic collisions) has not been detected by instruments such as Fermi-LAT, placing stringent upper limits on the cosmic-ray proton energy density in clusters (M. Ackermann et al. 2010; G. Brunetti et al. 2012; F. Zandanel, C. Pfrommer & F. Prada 2014; G. Brunetti, S. Zimmer & F. Zandanel 2017; R. Adam et al. 2021). Second, the hadronic model predicts a smoother and more centrally peaked radio morphology than what is typically observed for radio haloes (J. Donnert et al. 2010). Third, the hadronic model has difficulties in reproducing the observed bimodality in the radio-X-ray luminosity relation and fails to account for the existence of ultra-steep spectrum haloes ($\alpha \sim 1.5$–1.9, where $S_\nu \propto \nu^{-\alpha}$ and α is the spectral index used in this study) detected predominantly at low radio frequencies (R. Cassano, G. Brunetti & G. Setti 2006; G. Brunetti et al. 2008). These ultra-steep spectrum radio haloes (USSRHs), are therefore a crucial class of objects for discerning between different models of the radio halo formation mechanism. USSRH detections are limited to the relatively low redshift universe at present, and often have low signal-to-noise (SNR) ratios and limited fidelity.

Observations at high redshift are crucial for testing theoretical models, studying their evolution, and exploring their connection to the ICM. In particular, detections of USSRHs at higher redshift are important because turbulent re-acceleration models predict that haloes become rarer and fainter at earlier cosmic epochs (e.g. R. Cassano 2010; G. Brunetti & T. W. Jones 2014), when clusters are dynamically younger and inverse-Compton (IC) losses against the cosmic microwave background (CMB) are stronger (e.g. G. Brunetti & A. Lazarian 2007; R. Cassano et al. 2012, G. Di Gennaro et al. 2021). Finding USSRHs at high-z therefore provides unique constraints on the efficiency of particle re-acceleration, the role of cluster mergers, and the evolution of cluster magnetic fields over cosmic time.

In this Letter, we report the discovery of the most distant ultra-steep-spectrum radio halo (USSRH) known to date, detected in the MeerKAT-South Pole Telescope survey (UHF band) at the position of the galaxy cluster SPT-CLJ2337−5942. This SZ-selected cluster was first discovered by K. Vanderlinde et al. (2010) and lies within the South Pole Telescope (SPT) 100 square degree (deg^2) deep field (N. Huang et al. 2020). It has a redshift of $z = 0.78$ and a mass of $M_{500} = 8.32 \times 10^{14}\,\mathrm{M}_\odot$ (N. Huang et al. 2020), where M_{500} is the mass enclosed within a sphere of radius R_{500}, defined as the radius within which the average density is 500 times the critical density of the Universe at the cluster's redshift. This Letter is structured as follows: Section 2 briefly outlines the observations and data processing, Section 3 describes the discrete source subtraction technique and low-resolution high brightness temperature (T_B) imaging, Section 4

discusses the results, and Section 5 presents our conclusions. We adopt a ΛCDM flat cosmology with $H_0 = 70$ km s^{-1} Mpc^{-1}, $\Omega_m = 0.3$, and $\Omega_\Lambda = 0.7$. At the redshift of SPT-CLJ2337−5942 ($z = 0.78$), 1 arcsec corresponds to 7.42 kpc.

2 OBSERVATIONS AND DATA PROCESSING

2.1 MeerKAT observations

The radio observations were performed with the MeerKAT telescope, an array composed of 64 × 13.5 m antennas in the Northern Cape, South Africa. Approximately 70 per cent of the collecting area (48 antennas) is located in the central ∼ 1-km diameter core region, with the remainder spread out to longer baselines of up to 8 km (J. Jonas & MeerKAT Team 2016). This provides excellent brightness temperature sensitivity, while still retaining the ability to calibrate on and subtract out compact sources in the visibility domain. MeerKAT currently has three frequency bands (UHF: 0.58–1.09 GHz, *L* band: 0.9–1.7 GHz, *S* band: 1.75–3.5 GHz), with plans to extend to a fourth frequency band from 8.4 to 15.4 GHz.

The 100 deg^2 MeerKAT-South Pole Telescope Survey (Proposal ID:SCI-20220822-JV-02 and SCI-20230907-JV-01) was carried out in the UHF band and is centred on $\alpha = 23$h 30m, $\delta = -55°$. The survey is comprised of 78 pointings, each with a primary beam FWHM of ∼1.6 deg at 816 MHz. Each pointing was observed for ∼1 h, achieving a per-pointing depth of 10 μJy beam^{-1} and brightness temperature sensitivity of ∼258 mK, for Briggs-weighted (ROBUST = −0.5) images. The combined mosaic has a sensitivity of 14 μJy beam^{-1} when smoothed to a common resolution of 10.2 arcsec. The total survey observation time was 116 h and used an 8-s integration time in the 32k correlator mode set-up, resulting in 32 768 channels, each 16.602 kHz wide. The combined data volume is approximately ∼250 TB. Out of 64 MeerKAT antennas, 60 were typically available for each pointing. The sources J0408−6545 (primary calibrator) and J2329−4730 (secondary calibrator) were used for absolute flux, bandpass, phase, and complex gain calibration.

2.2 Calibration and imaging

We processed the MeerKAT data with the OXKAT pipeline (I. Heywood 2020) in combination with modified scripts of procedures of our own. OXKAT is a set of PYTHON-based scripts that semi-automatically process Stokes I MeerKAT data, including direction-dependent calibration, which is essential for our large field-of-view, sensitivity, and $\lesssim$1 GHz observing frequency. Outlined below is a brief description of the steps we performed using the OXKAT pipeline.

The MeerKAT UHF-band data were processed using a combination of standard and advanced calibration techniques. First-generation calibration (1GC) was performed using the OXKAT pipeline in CASA (J. P. McMullin et al. 2007), reducing the number of channels from 32 768 (32k) to 1024 (1k). After initial flagging for radio frequency interference, calibration solutions from primary and secondary calibrators were applied to the target field. The data were imaged using WSCLEAN (A. R. Offringa et al. 2014), producing 10k × 10k pixel maps of the full bandwidth, as well as eight sub-band images (68 MHz each) utilizing Briggs weighting, with (ROBUST) parameters of −0.5 and 0.0.

Direction independent self-calibration (2GC) was conducted with CUBICAL (J. S. Kenyon et al. 2018) for delay and phase-only calibration, followed by amplitude and phase calibration using an iterative process of imaging and model prediction. The mask from the 1GC imaging was iteratively refined, for subsequent rounds of imaging. For direction-dependent effect corrections, we begin by 'peeling' bright off-axis sources, which are numerous at UHF frequencies, coupled with the larger field of view. The peeling process involves phase-rotation and solving for gain terms using CUBICAL, with problematic sources iteratively uv-subtracted from the visibility data. Finally, facet-based DDE corrections were applied using DDFACET (C. Tasse et al. 2018) and KILLMS (C. Tasse 2014; O. M. Smirnov & C. Tasse 2015), dividing the sky model into multiple directions and solving for complex gains per facet. DDFACET was then used to apply the latter complex gain corrections on the fly, producing a direction-dependent calibrated (3GC) image with reduced artefacts around bright sources.

3 ISOLATING DIFFUSE RADIO EMISSION

We identified the diffuse source through a systematic manual search for extended radio emission in the sample of 89 SPTpol galaxy clusters (N. Huang et al. 2020) that lie within the MeerKAT-SPT 100 deg^2 field. In this programme, each SZ-selected cluster was inspected for large-scale, low-surface-brightness radio features after compact sources were modelled and subtracted. The target discussed here revealed a clear excess of diffuse emission, consistent in extent and morphology with a radio halo.

To measure the integrated flux density of the diffuse emission, we must first subtract point sources in close proximity. This step, performed in the visibility domain, is essential to ensure that the flux density measurements of the diffuse emission were not contaminated by the embedded compact sources. Additionally, removing the point sources reduces blending with the extended emission when producing lower resolution maps better matched to the emission scales of interest. Point source subtraction was performed using CRYSTALBALL[1] package which utilizes a source list from WSCLEAN to generate visibilities containing only the identified point sources. The CASA UVSUB task is then used to subtract these from the calibrated visibilities. We used these modified visibilities and modified imaging weights to produce lower resolution maps with higher brightness temperature sensitivity that enhance the diffuse radio emission SNR, as follows.

To locate diffuse radio emission in our target field, we take advantage of MeerKAT's pinched core antenna configuration. At 816 MHz, short baselines within the dense core are sensitive to extended sources ($\gtrsim$1 arcmin), while longer baselines are used to identify and accurately subtract point sources. We impose a baseline-length lower limit (uv-range > 10 kλ) to carry out point-source substraction. The model from this image is used to create a point-source-subtracted image thereby isolating the diffuse emission.

A lower-resolution, higher brightness temperature sensitivity image was obtained by restricting the uv-range between 0–2 kλ and using a Briggs ROBUST = 0.0 in DDFACET, resulting in PSF FWHM dimensions of 12.7 arcsec × 9.9 arcsec. This image, with imaging weights closer to natural weighting, is better optimized to highlight extended diffuse emission. For brevity, we refer to this as the 'high-T_B image' for the remainder of the paper.

The flux densities and their uncertainties were calculated using the RADIOFLUX[2] tool, which measures integrated fluxes by summing pixel values within user-defined source regions on the images. The regions were defined to encompass compact sources in the

[1] https://github.com/caracal-pipeline/crystalball
[2] https://github.com/mhardcastle/radioflux

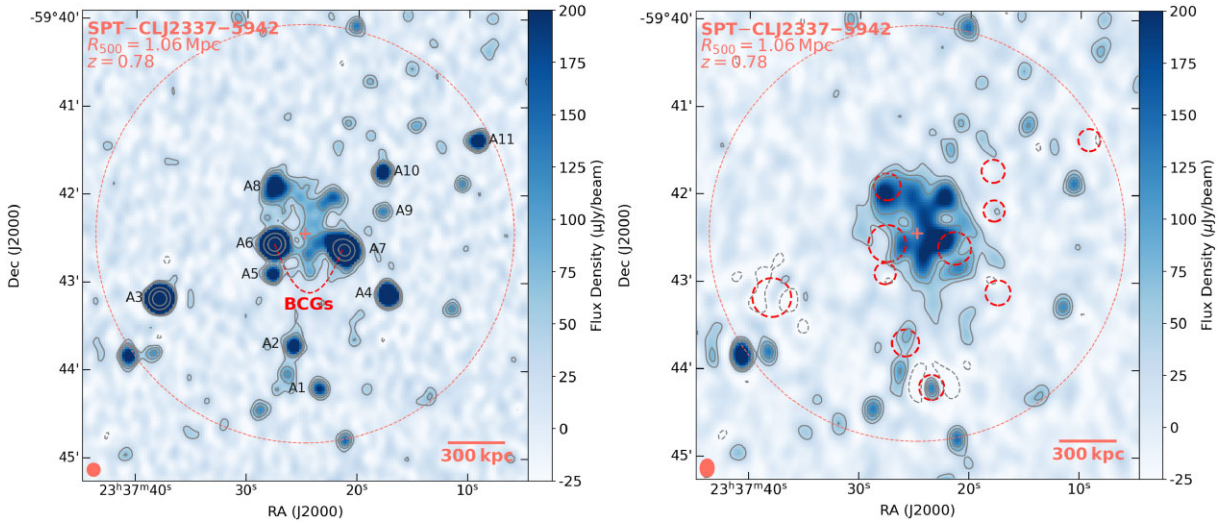

Figure 1. Left: MeerKAT 816 MHz image of SPT-CLJ2337−5942 at ROBUST −0.5, with a resolution of 8.9 arcsec × 8.9 arcsec and position angle of 0.0 degree. Contour levels are drawn at $[-5, 5, 9, 13, 17] \times 1\sigma$, where $\sigma = 9.15$ μJy beam^{-1}. The labels A1–A11 (including the two BCGs) indicate the compact sources within the R_{500} cluster region (bigger circle). Right: Lower resolution (high-T_B) MeerKAT 816 MHz image of SPT-CLJ2337−5942 with discrete sources (denoted by small circles) subtracted, at ROBUST 0.0, with a resolution of 12.6 arcsec × 9.9 arcsec and position angle of −2.17 degrees. Contour levels are drawn at $[-5, 5, 9, 13, 17] \times 1\sigma$, where $\sigma = 7.50$ μJy beam^{-1}, with negative contours shown as dashed lines. The cluster centre is marked by a cross. The synthesized beams for both images are shown in the lower left corners.

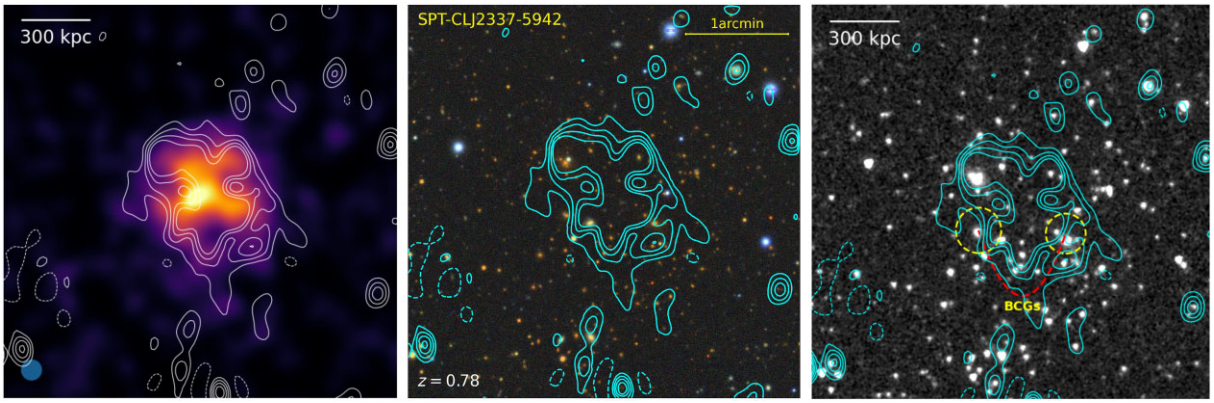

Figure 2. Left: *Chandra* X-ray image of SPT-CLJ2337−5942 in the 0.5–2.0 keV band, smoothed to 12 arcsec. The Gaussian smoothing kernel FWHM is indicated in the bottom-left corner. The radio halo emission is shown as white (teal) contours in the left (right) panel, with levels at $[-5, 5, 9, 13, 17] \times 1\sigma$, where $\sigma = 7.50$ μJy beam^{-1}. The emission traces the brightness peak and exhibits a filamentary morphology. Middle: Optical grz image of SPT-CLJ2337−5942 from the DESI-Legacy-Surveys. The radio halo overlaps with two bright galaxies which are possible BCGs (e.g. K. Andersson et al. 2011) counterparts embedded in the halo. Right: *Spitzer*/IRAC 3.6 μm image (M. L. N. Ashby et al. 2013) with MeerKAT contours, highlighting the overdensity of mid-infrared (MIR)-detected cluster galaxies. The IRAC panel also shows that several compact radio peaks have IR counterparts, while the diffuse radio halo emission extends over the same region as the cluster galaxy distribution.

full-resolution (8 arcsec) image and diffuse emission in the lower resolution high-T_B (12.6 arcsec × 9.9 arcsec) image.

4 RESULTS AND DISCUSSION

The MeerKAT UHF-band high-T_B image reveals extended diffuse emission detected with high confidence at the centre of SPT-CLJ2337−5942. The largest linear size is ∼800 kpc at 816 MHz and has a complex morphology (see Fig. 1). We compare this radio image with a *Chandra* X-ray 0.5–2 keV image, obtained from archival *Chandra* ACIS-I data (ObsID 11859; PI: Garmire) with a total exposure time of 19.77 ksec. As seen in Fig. 2, the diffuse radio emission has a very similar morphological structure to the *Chandra* X-ray emission, presumed to trace the ICM. Based on the cluster location, the close correspondence between diffuse X-ray and radio emission, we classify this diffuse emission as a radio halo. The basic properties of the cluster are presented in Table 1.

Table 1. Properties of SPT-CLJ2337−5942. X-ray properties are adopted from K. Andersson et al. (2011).

R.A.$_{J2000}$ (^{h}:^{m}:^{s})	23:37:24.2
Dec.$_{J2000}$ ($^\circ$:$'$:$''$)	−59:42:17
Redshift (z)	0.78
M_{500c} (10^{14} M$_\odot$)	8.32 ± 0.82
$L_{x,500}$ (10^{44} erg s^{-1})	8.9 ± 0.5
P_{816} (10^{24} W Hz^{-1})	2.5 ± 0.2

Table 2. The properties of the compact sources within the R_{500} cluster region. BCG denotes BCGs, whereas CM denotes cluster members. FG and BG denote foreground and background galaxies, respectively.

ID	RA (J2000) (^{h}:^{m}:^{s})	Dec (J2000) ($^{\circ}$:$'$:$''$)	$z_{\rm phot}$	Flux (mJy)	Notes
A1	23:37:17	−59:43:08	0.76	0.83 ± 0.02	CM
A2	23:37:38	−59:43:11	0.78	6.7 ± 0.03	CM
A3	23:37:26	−59:43:43	0.27	0.36 ± 0.02	FG
A4	23:37:18	−59:42:12	0.76	0.12 ± 0.02	CM
A5	23:37:23	−59:44:13	1.2	0.22 ± 0.02	BG
A6	23:37:28	−59:42:33	0.78	6.6 ± 0.03	BCG
A7	23:37:21	−59:42:37	0.81	5.8 ± 0.03	BCG
A8	23:37:27	−59:41:54	0.97	0.57 ± 0.02	BG
A9	23:37:16	−59:42:10	0.84	0.26 ± 0.02	BG
A10	23:37:15	−59:41:43	1.0	0.34 ± 0.02	BG
A11	23:37:07	−59:41:22	1.0	0.34 ± 0.02	BG

An optical RGB image (*grz*-band) from DESI Legacy Survey (A. Dey et al. 2019), shown in Fig. 2, shows that SPT-CLJ2337−5942 hosts two brightest cluster galaxies (BCGs) and multiple sub-groups undergoing collision with the radio halo, further reinforcing its classification as a merging cluster (disturbed). Z. S. Yuan & J. L. Han (2020) and Z. S. Yuan, J. L. Han & Z. L. Wen (2022) confirmed that SPT-CLJ2337−5942 is a disturbed galaxy cluster based on its X-ray morphology. The optical and infrared (IR) images (see Fig. 2) further highlight the galaxy distribution, which appears elongated along the merger axis and consistent with the disturbed morphology of the system. Within the $R_{500} = 1.1$ Mpc radius, we identify eleven compact radio sources in our 816 MHz full-resolution image (labelled A1–A11 in Fig. 1). Of these, five are confirmed as cluster members (including the two BCGs), five are associated with background galaxies ($z > 0.8$), and one is a foreground galaxy ($z \sim 0.272$), based on photometric redshifts from the DESI Legacy Imaging Surveys Data (DR8; K. J. Duncan 2022). The properties of these compact sources are detailed in Table 2.

The halo shows an overall smooth, diffuse morphology, but with noticeable filamentary substructures that trace the thermal X-ray emission of the ICM, as shown in Fig. 2. The striking spatial correlation between the diffuse synchrotron emission and the X-ray brightness strongly supports a scenario in which both components arise from the same large-scale turbulent environment. In this framework, ICM turbulence-driven by cluster mergers both heats the ICM gas and re-accelerates cosmic-ray electrons, with magnetic fields permeating the ICM enabling synchrotron emission across the X-ray-emitting volume (e.g. G. Brunetti & T. W. Jones 2014). This interpretation is supported by quantitative studies that report point-to-point correlations between radio and X-ray surface brightness in several clusters hosting radio haloes (e.g. L. Feretti et al. 2001; F. Govoni et al. 2001; S. Giacintucci et al. 2005; S. Brown & L. Rudnick 2011; K. Rajpurohit et al. 2018) and it is self-evident that the point-to-point correlation in SPT-CLJ2337−5942 is very high. However, exceptions exist where no such correlation is found (e.g. T. W. Shimwell et al. 2014), highlighting the complexity of radio-X-ray connections in the ICM and the importance of deep, high-fidelity radio imaging.

We quantified the radio-X-ray connection by performing a pixel-by-pixel correlation analysis between the reprojected maps (Figure not shown). We find a strong Pearson correlation coefficient of $r = 0.73$ (ρ-value $\ll 10^{-10}$) and a Spearman rank correlation coefficient of $\rho = 0.50$, both indicating a highly significant correlation between the diffuse radio and thermal X-ray surface brightness.

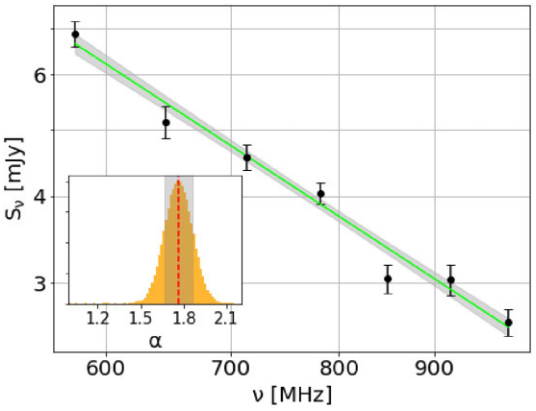

Figure 3. Integrated radio spectrum of the halo between $\nu = 578$–986 MHz. The points show the measured flux densities with 1σ uncertainties. The green line indicates the median posterior-fit power law derived from an MCMC sampler (D. Foreman-Mackey et al. 2013), with the shaded region representing the 68 per cent confidence intervals. The integrated spectral index is $\alpha = 1.76 \pm 0.10$, classifying the source as an USSRH. The inset in the bottom-left corner shows the posterior probability distribution of α derived from the MCMC sampling.

Fitting a power law of the form $I_{\rm radio} \propto I_X^b$, we obtain the best-fitting slope of $b = 0.72 \pm 0.02$. This slope is fully consistent with point-to-point correlations measured in other clusters hosting radio haloes (e.g. L. Feretti et al. 2001; F. Govoni et al. 2001; S. Giacintucci et al. 2005; S. Brown & L. Rudnick 2011; K. Rajpurohit et al. 2018), further reinforcing the picture that the radio and X-ray emission in SPT-CLJ2337−5942 trace the same turbulent ICM volume.

Additionally, there appear to be low-brightness depressions in the X-ray emission that resemble cavities. These are unlikely to be AGN-inflated bubbles, given the absence of appropriately located compact radio cores, jets, or optical AGN features. Alternatively, these structures can be interpreted as merger-induced low-density regions shaped by bulk ICM motions or turbulence (e.g. M. Markevitch & A. Vikhlinin 2007; F. Vazza et al. 2009; J. A. ZuHone, M. Markevitch & D. Lee 2011). The latter is consistent with the radio halo scenario, in which the synchrotron-emitting electrons are re-accelerated over large volumes without requiring ongoing AGN activity, particularly in post-merger or dynamically evolved systems (e.g. G. Brunetti et al. 2008).

The flux density of the radio halo is measured as $S_{816} = 4.34 \pm 0.41$ mJy. From sub-band image flux density measurements, we calculate the integrated spectral index of the radio halo to be $\alpha \sim 1.76 \pm 0.10$ (between $\nu = 578$–986 MHz) using a Markov chain Monte Carlo (MCMC) sampler (D. Foreman-Mackey et al. 2013). The integrated spectral index posterior probability distribution function (PDF, see Fig. 3) identifies the halo as an USSRH with high confidence. As discussed in Section 1, this is a rare type of halo, particularly at $z \gtrsim 0.5$. USSRHs are thought to trace non-thermal emission from aged relativistic electron populations re-energized by turbulence generated during less energetic cluster mergers such as minor mergers, mergers between lower mass systems, or mergers occurring at higher redshift (e.g. R. Cassano et al. 2006, 2010; G. Brunetti et al. 2008; R. Cassano 2010; G. Brunetti & T. W. Jones 2014). In such conditions, the reduced turbulent energy available leads to inefficient particle acceleration and hence much steeper radio spectra. These haloes typically exhibit low surface brightness (e.g. R. J. Weeren et al. 2019), consistent with SPT-CLJ2337−5942, for which we estimate a surface brightness of $\sim$0.4 μJy arcsec^{-2},

which is in line with expectations (e.g. M. Pandey-Pommier et al. ; K. Rajpurohit et al. 2023; R. Santra et al. 2024). This low surface brightness, combined with their steep spectra, often causes USSRHs to be missed in wide-area surveys, as they require highly sensitive, high-fidelity images at frequencies $\upsilon \lesssim 1$ GHz. SPT-CLJ2337−5942 is the most distant USSRH known to date, at a redshift of $z = 0.78$. This detection therefore demonstrates that the sensitivity and image fidelity of the MeerKAT UHF band can reveal distant USSRHs in relatively short observations (∼1 h), enabling large-area surveys conducive to the discovery of rare systems such as this. At the same time, the discovery within a 100 deg^2 area suggests that USSRHs could be more common than the current total sample (∼10) indicates, though this may depend on observational sensitivity and selection effects (e.g. R. Cassano et al. 2012; T. Pasini et al. 2024).

Using the integrated flux density and spectral index of the halo, we estimate a radio power of approximately $P_{1.4} = 9.6 \pm 0.9 \times 10^{23}$ W Hz^{-1}, scaled from the observed frequency of 816 MHz assuming the in-band spectral index. At high redshifts, relativistic electrons experience enhanced energy losses due to IC scattering with the increasingly dense CMB photon field. This process shortens their radiative lifetimes and suppresses the power and detectability of synchrotron-emitting regions (e.g. C. Ferrari et al. 2008; R. Cassano et al. 2010; R. R. Lindner et al. 2014; F. Sweijen et al. 2022).

We compare this radio power to the sample of known USSRHs ($z \sim 0.048$–0.5), confirmed by multiband radio detections reported in the literature. This is a statistically small yet instructive sample, including Abell 1132 (A. Wilber et al. 2018), Abell 1550 (T. Pasini et al. 2022), MACS J1149 (L. Bruno et al. 2021), A521 (R. Santra et al. 2024), RXCJ1514.9−1523 (S. Giacintucci et al. 2011), Abell 2142 (L. Bruno et al. 2023), Abell 697 (G. Macario et al. 2010), Abell 3404 (S. W. Duchesne et al. 2021), Abell 2256 (K. Rajpurohit et al. 2023), Abell 1033 (H. W. Edler et al. 2022), and A3562 (T. Venturi et al. 2022), along with the source presented in this work. The $P_{1.4}$–M_{500} scaling relation (see Fig. 4) shows that the USSRH radio power lies within the scatter of both nearby and distant USSRH populations, occupying a region below the ordinary halo correlation. By normalizing halo power by cluster mass, we can test whether our system is unusual compared to known USSRHs. Fig. 4 further illustrates that while most USSRHs are found at $z \lesssim 0.5$, our detection at $z \sim 0.78$ extends this population to much higher redshift. Its $P_{1.4}/M_{500}$ ratio is consistent with lower-z USSRHs, indicating that the underlying particle acceleration mechanisms remain comparably efficient out to cosmological lookback time of ∼7 Gyr.

Assuming turbulent re-acceleration remains the dominant mechanism (G. Brunetti et al. 2001; R. Cassano et al. 2006; G. Brunetti et al. 2008; R. Cassano et al. 2010; G. Brunetti & T. W. Jones 2014), such a trend would suggest that stronger magnetic fields and enhanced turbulence are required at higher redshifts (G. Di Gennaro et al. 2025). This is particularly relevant given that IC losses increase with redshift (e.g. C. Ferrari et al. 2008; R. Cassano et al. 2010; R. R. Lindner et al. 2014), reducing the efficiency of synchrotron emission. Thus, sustaining radio halo luminosities comparable to low-redshift systems (G. Macario et al. 2010; S. Giacintucci et al. 2011; A. Wilber et al. 2018; S. W. Duchesne et al. 2021; H. W. Edler et al. 2022; T. Pasini et al. 2022; T. Venturi et al. 2022; L. Bruno et al. 2023; K. Rajpurohit et al. 2023; R. Santra et al. 2024) would necessitate a greater injection of turbulent energy or elevated magnetic field strengths in high-z clusters, as anticipated by turbulent re-acceleration models (e.g. G. Di Gennaro et al. 2021). This is shown in Fig. 4, where the best-fitting line is based on the scaling relation studies of USSRHs conducted by V. Cuciti et al. (2021b), following the fitting procedure outlined in R. Cassano et al. (2013). The scaling relation further supports the USSRH classification, as the halo appears radio underluminous in comparison to the correlation reported by V. Cuciti et al. (2021b) between 1.4 GHz radio power and the cluster mass.The detection of the USSRH in SPT-CLJ2337−5942 provides compelling evidence in favour of the turbulent re-acceleration model over the hadronic scenario (e.g. B. Dennison 1980; P. Blasi & S. Colafrancesco 1999; G. Brunetti 2004), consistent with predictions that steep-spectrum haloes arise from turbulence-driven acceleration in the ICM. In merging clusters, steep-spectrum haloes are predicted to result from turbulence-driven acceleration of relativistic electrons (G. Brunetti et al. 2001; G. Brunetti & T. W. Jones 2014), and ongoing/forthcoming low-frequency arrays, together with wide-field, high-fidelity surveys like MeerKAT-SPT, will enable observational tests of these theoretical predictions (e.g. G. Macario et al. 2010; R. Cassano et al. 2012; T. Pasini et al. 2024).

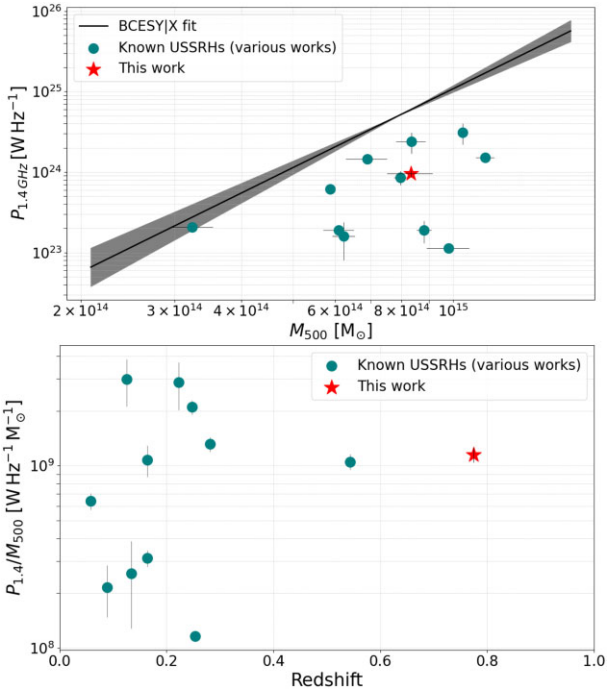

Figure 4. Top: The $P_{1.4\,\mathrm{GHz}}$–M_{500} scaling relation of known USSRHs (G. Macario et al. 2010; S. Giacintucci et al. 2011; A. Wilber et al. 2018; L. Bruno et al. 2021; S. W. Duchesne et al. 2021; H. W. Edler et al. 2022; T. Pasini et al. 2022; T. Venturi et al. 2022; L. Bruno et al. 2023; K. Rajpurohit et al. 2023; R. Santra et al. 2024). The USSRH presented in this work is marked with a red star. The solid line represents the correlation for normal and USSRHs, as reported by V. Cuciti et al. (2021b). Bottom: Radio power at 1.4 GHz normalized by cluster mass, $P_{1.4}/M_{500}$, for known USSRHs as a function of redshift.

5 CONCLUSION

In this Letter, we present MeerKAT UHF-band observations of the galaxy cluster SPT-CLJ2337−5942 at $z = 0.78$. The high-T_B images reveal an USSRH within the cluster, marking the highest redshift for an USSRH reported to date. These are important systems that enable us to discern between radio halo formation models, and SPT-CLJ2337−5942 has two key traits in this regard:

(i) An integrated spectral index of $\alpha \sim 1.76 \pm 0.10$ (578–986 MHz), significantly steeper than that predicted by hadronic models, indicating that ongoing particle re-acceleration is necessary.

(ii) A striking spatial correlation between the filamentary-like diffuse radio emission and the X-ray brightness, implying a direct link between thermal ICM electrons, non-thermal electrons, and cluster magnetic fields.

This USSRH has a radio power of $P_{1.4} = 9.6 \pm 0.9 \times 10^{23}\,\mathrm{W\,Hz^{-1}}$. According to the $P_{1.4}$–M_{500} scaling relation, the USSRH appears underluminous, as it may result from less energetic phenomena, such as minor cluster mergers within more massive systems (e.g. R. Cassano et al. 2008a; R. Cassano 2010). These processes typically lead to less luminous steep spectrum haloes ($\alpha > 1.5$). Given the steep spectrum of the USSRH in SPT-CLJ2337−5942, a hadronic origin for the halo is unlikely. Instead, turbulence re-acceleration is likely the primary mechanism for halo production, with the necessary energy for this re-acceleration expected to be supplied by cluster merger events. Future observations with the SKA, together with ongoing low-frequency surveys such as MeerKAT-SPT, will significantly expand the sample of high-redshift USSRHs, enabling more robust tests of radio halo formation models and particle acceleration mechanisms.

ACKNOWLEDGEMENTS

We thank the anonymous referee for their helpful comments which improved the paper. Isaac Selaelo Magolego (ISM), Roger Paul Deane (RPD), and William Rasakanya (WR) acknowledge the financial support of the South African Radio Astronomy Observatory (SARAO) for this research. The MeerKAT telescope is operated by SARAO, a facility of the National Research Foundation (NRF), which is an agency under the Department of Science, Technology and Innovation (DSI). We also express our gratitude to the SARAO science commissioning and operations team, led by Sharmila Goedhart, for their assistance. We also acknowledge the use of the ilifu cloud computing facility (www.ilifu.ac.za), a partnership between the University of Cape Town, the University of the Western Cape, Stellenbosch University, Sol Plaatje University, and the Cape Peninsula University of Technology. The ilifu facility is supported by contributions from the Inter-University Institute for Data Intensive Astronomy (IDIA), a partnership between the University of Cape Town, the University of Pretoria, and the University of the Western Cape; the Computational Biology division at UCT; and the Data Intensive Research Initiative of South Africa (DIRISA). Manuel Aravena (MA) is supported by Fondo Nacional de Desarrollo Científico y Tecnológico (FONDECYT) grant no. 1252054, and gratefully acknowledges support from Agencia Nacional de Investigación y Desarrollo (ANID) Basal Project FB210003 and ANID MILENIO NCN2024_112.

Additionally, this work made use of the CARTA (Cube Analysis and Rendering Tool for Astronomy) software (DOI: 10.5281/zenodo.3377984 – https://cartavis.github.io).

DATA AVAILABILITY

The MeerKAT raw data used in this study are publicly available (Project IDs SCI-20220822-JV-02 and SCI-20230907-JV-01) in accordance with the South African Radio Astronomy Observatory data release policy, while calibrated and advanced data products are available upon reasonable request.

REFERENCES

Ackermann M. et al., 2010, Phys. Rev. D, 82, 092004
Adam R., Goksu H., Brown S., Rudnick L., Ferrari C., 2021, A&A, 648, A60
Andersson K. et al., 2011, ApJ, 738, 48
Aragón-Calvo M. A., Van De Weygaert R., Jones B. J. T., 2010, MNRAS, 408, 2163
Ashby M. L. N. et al., 2013, ApJS, 209, 22
Bagchi J., Enßlin T. A., Miniati F., Stalin C. S., Singh M., Raychaudhury S., Humeshkar N. B., 2002, New Astron., 7, 249
Blasi P., Colafrancesco S., 1999, Astropart. Phys., 12, 169
Blumenthal G. R., Faber S. M., Primack J. R., Rees M. J., 1984, Nature, 311, 517
Botteon A., Brunetti G., Ryu D., Roh S., 2020, A&A, 634, A64
Brown S., Rudnick L., 2011, MNRAS, 412, 2
Brunetti G., 2004, J. Korean Astron. Soc., 37, 493
Brunetti G., Blasi P., 2005, MNRAS, 363, 1173
Brunetti G., Jones T. W., 2014, Int. J. Mod. Phys. D, 23, 1430007
Brunetti G., Lazarian A., 2007, MNRAS, 378, 245
Brunetti G., Lazarian A., 2011, MNRAS, 410, 127
Brunetti G., Setti G., Feretti L., Giovannini G., 2001, MNRAS, 320
Brunetti G. et al., 2008, Nature, 455, 944
Brunetti G., Blasi P., Reimer O., Rudnick L., Bonafede A., Brown S., 2012, MNRAS, 426, 956
Brunetti G., Zimmer S., Zandanel F., 2017, MNRAS, 472, 1506
Bruno L. et al., 2021, A&A, 650, A44
Bruno L. et al., 2023, A&A, 678, A133
Cassano R., 2010, A&A, 517, A10
Cassano R., Brunetti G., 2005, MNRAS, 357, 1313
Cassano R., Brunetti G., Setti G., 2006, MNRAS, 369, 1577
Cassano R., Brunetti G., Venturi T., Setti G., Dallacasa D., Giacintucci S., Bardelli S., 2008a, A&A, 480, 687
Cassano R., Gitti M., Brunetti G., 2008b, A&A, 486, L31
Cassano R., Brunetti G., Röttgering H. J. A., Brüggen M., 2010, A&A, 509, A68
Cassano R., Brunetti G., Norris R. P., Röttgering H. J. A., Johnston-Hollitt M., Trasatti M., 2012, A&A, 548, A100
Cassano R. et al., 2013, ApJ, 777, 141
Cassano R. et al., 2023, A&A, 672, A43
Cautun M., van de Weygaert R., Jones B. J. T., Frenk C. S., 2014, MNRAS, 441, 2923
Cuciti V. et al., 2021a, A&A, 647, A50
Cuciti V. et al., 2021b, A&A, 647, A51
Dasadia S. et al., 2016, ApJ, 820, L20
Dennison B., 1980, ApJ, 239, L93
Dey A. et al., 2019, AJ, 157, 168
Di Gennaro G. et al., 2021, Nat. Astron., 5, 268
Di Gennaro G. et al., 2025, A&A, 695, A215
Donnert J., Dolag K., Cassano R., Brunetti G., 2010, MNRAS, 407, 1565
Duchesne S. W., Johnston-Hollitt M., Wilber A. G., 2021, Publ. Astron. Soc. Aust., 38, e031
Duncan K. J., 2022, MNRAS, 512, 3662
Edler H. W. et al., 2022, A&A, 666, A3
Ensslin T., Biermann P., Klein U., Kohle S., 1998, A&A, 332, 395
Feretti L., Fusco-Femiano R., Giovannini G., Govoni F., 2001, A&A, 373, 106
Feretti L., Giovannini G., Govoni F., Murgia M., 2012, A&AR, 20, 54
Ferrari C., Govoni F., Schindler S., Bykov A. M., Rephaeli Y., 2008, Space Sci. Rev., 134, 93
Foreman-Mackey D., Hogg D. W., Lang D., Goodman J., 2013, PASP, 125, 306
Giacintucci S. et al., 2005, A&A, 440, 867

Giacintucci S., Dallacasa D., Venturi T., Brunetti G., Cassano R., Markevitch M., Athreya R. M., 2011, A&A, 534, A57
Govoni F., Feretti L., Giovannini G., Böhringer H., Reiprich T. H., Murgia M., 2001, A&A, 376, 803
Heywood I., 2020, oxkat: Semi-automated imaging of MeerKAT observations, preprint (ascl:2009.003)
Huang N. et al., 2020, AJ, 159, 110
Jonas J., MeerKAT Team, 2016, Proc. Sci., MeerKAT Science: On the Pathway to the SKA (MeerKAT2016). SISSA, Trieste, PoS#1
Jones C., Forman W., 1999, ApJ, 511, 65
Kenyon J. S., Smirnov O. M., Grobler T. L., Perkins S. J., 2018, MNRAS, 478, 2399
Lindner R. R. et al., 2014, ApJ, 786, 49
Macario G., Venturi T., Brunetti G., Dallacasa D., Giacintucci S., Cassano R., Bardelli S., Athreya R., 2010, A&A, 517, A43
Macario G., Markevitch M., Giacintucci S., Brunetti G., Venturi T., Murray S. S., 2011, ApJ, 728, 82
Malavasi N., Aghanim N., Tanimura H., Bonjean V., Douspis M., 2020, A&A, 634, A30
Mann A. W., Ebeling H., 2012, MNRAS, 420, 2120
Markevitch M., Vikhlinin A., 2007, Phys. Rep., 443, 1
McMullin J. P., Waters B., Schiebel D., Young W., Golap K., 2007, in Shaw R. A., Hill F., Bell D. J., eds, ASP Conf. Ser. Vol. 376, Astronomical Data Analysis Software and Systems XVI. Astron. Soc. Pac., San Francisco, p. 127
Miniati F., 2015, ApJ, 800, 60
Nishiwaki K., Asano K., 2022, ApJ, 934, 182
Offringa A. R. et al., 2014, MNRAS, 444, 606
Osinga E. et al., 2025, A&A, 694, A44
Pandey-Pommier M. et al. 2016, SF2A-2016, 367
Pasini T. et al., 2022, A&A, 663, A105
Pasini T. et al., 2024, A&A, 689, A218
Petrosian V., 2001, ApJ, 557, 560
Phuravhathu D. G. et al., 2025, MNRAS, 542, 1544
Rajpurohit K. et al., 2018, ApJ, 852, 65
Rajpurohit K. et al., 2023, A&A, 669, A1
Roettiger K., Burns J. O., Stone J. M., 1999, ApJ, 518, 603
Russell H. R. et al., 2011, MNRAS, 417, L1
Santra R. et al., 2024, ApJ, 962, 40
Santra R. et al., 2024, ApJ, 976, 66
Shimwell T. W., Brown S., Feain I. J., Feretti L., Gaensler B. M., Lage C., 2014, MNRAS, 440, 2901
Smirnov O. M., Tasse C., 2015, MNRAS, 449, 2668
Sweijen F. et al., 2022, A&A, 658, A3
Tasse C., 2014, A&A, 566, A127
Tasse C. et al., 2018, A&A, 611, A87
Vanderlinde K. et al., 2010, ApJ, 722, 1180
Vazza F., Brunetti G., Kritsuk A., Wagner R., Gheller C., Norman M., 2009, A&A, 504, 33
Venturi T. et al., 2022, A&A, 660, A81
Vikhlinin A., Kravtsov A., Forman W., Jones C., Markevitch M., Murray S. S., Van Speybroeck L., 2006, ApJ, 640, 691
van Weeren R. J., Röttgering H. J. A., Brüggen M., Hoeft M., 2010, Science, 330, 347
van Weeren R. J., de Gasperin F., Akamatsu H., Brüggen M., Feretti L., Kang H., Stroe A., Zandanel F., 2019, Space Sci. Rev., 215, 16
White D. A., Fabian A. C., 1995, MNRAS, 273, 72
Whittingham J., Pfrommer C., Werhahn M., Jlassi L., Girichidis P., 2024, preprint (arXiv:2411.11947)
Wilber A. et al., 2018, MNRAS, 473, 3536
Wittor D., Ettori S., Vazza F., Rajpurohit K., Hoeft M., Domínguez-Fernández P., 2021, MNRAS, 506, 396
Yuan Z. S., Han J. L., 2020, MNRAS, 497, 5485
Yuan Z. S., Han J. L., Wen Z. L., 2015, ApJ, 813, 77
Yuan Z. S., Han J. L., Wen Z. L., 2022, MNRAS, 513, 3013
Zandanel F., Pfrommer C., Prada F., 2014, MNRAS, 438, 124
ZuHone J. A., Markevitch M., Lee D., 2011, ApJ, 743, 16
Phuravhathu Dakalo G, Hilton M, Sikhosana S P, Perrott Y C, Mroczkowski T, Di Mascolo L, Klutse D Y, Knowles K, van Marrewijk J, Moodley K, Partridge B, Sifón C, Sureshkumar U, Wollack E J, 2025. Monthly Notices of the Royal Astronomical Society, 542, 1544

This paper has been typeset from a TEX/LATEX file prepared by the author.